Theoretical and experimental investigation of the electronic properties of the wide band-gap transparent semiconductor $MgGa_2O_4$

B. Thielert,[1] C. Janowitz,[1] Z. Galazka,[2] and M. Mulazzi[1,2]
[1]*Humboldt-Universität zu Berlin, Institut für Physik, Newtonstr. 15, D-12489 Berlin, Germany*
[2]*Leibniz-Institut für Kristallzüchtung, Max-Born-Str. 2, D-12489 Berlin, Germany*

(Received 21 December 2017; revised manuscript received 26 March 2018; published 14 June 2018)

We present an experimental and theoretical study of the electronic structure of the transparent conductive oxide semiconductor $MgGa_2O_4$. Its valence band and the core levels have been measured experimentally by angle-resolved photoemission spectroscopy and compared to theoretical *ab initio* density-functional calculations. The bands stem from oxygen orbitals and have a dispersion of about 0.6 eV and high effective masses, in agreement with the calculations. Angle-resolved measurements of the Ga 3*d* core levels indicate a sizable upward band bending, which in combination with an exact model potential yielded a quantitative estimate of the spatial extension of the depletion region, the effective Debye length in the material, and the extrinsic bulk carrier density.

DOI: 10.1103/PhysRevB.97.235309

I. INTRODUCTION

Transparent conductive oxides (TCOs) are interesting materials from the fundamental point of view because their physical behavior clashes with our intuition about the electronic structure of bulk matter. In fact, they possess at the same time semiconductorlike electrical conductivity and transparency in the visible range, two mutually exclusive properties in bulk intrinsic undoped semiconductors. This rather simple description of the fundamental properties of TCOs is complicated by the presence of extrinsic volume defects, surface states, and defects, which introduce electronic states in the band gap and therefore alter the light absorption spectrum and the electrical conduction.

A large number of angle-resolved photoemission spectroscopy (ARPES) studies has been devoted to the investigation of the many TCO family members: ZnO [1–4], CdO [5–7], In_2O_3 [8–10], and $SrTiO_3$ [11,12]. A further TCO interesting for applications is β-Ga_2O_3, which, thanks to its 4.85 eV band gap [13–16], has a very high breakdown voltage [17] and is seen as one of the most promising candidates for replacing present materials in high-power devices in the automotive and power transmission devices [18]. However, despite the promising properties, Ga_2O_3 has the disadvantage of crystallizing in a monoclinic unit cell [19], which has a strong mechanical anisotropy. The unfavorable consequence is that it is very difficult to fabricate large wafers oriented perpendicular to the (100) and (001) cleavage planes.

Therefore, materials with a wide band gap as Ga_2O_3, but with a more symmetric unit cell and a lattice parameter matched to that of other TCOs, are strongly sought after to grow functional epitaxial homo- or heterostructures. In this paper, we report a comprehensive study of the electronic structure of magnesium gallate, $MgGa_2O_4$, which is a TCO possessing the typical properties of this group: *n*-type conductivity in unintentionally doped as-grown crystals and optical and electrical conduction tuned by the growth and postgrowth annealing conditions [20]. As-grown $MgGa_2O_4$ crystals are blue and semiconducting with a relatively high carrier density, but annealing in oxygen renders them completely transparent and electrically insulating. On the other hand, annealing in vacuum and/or hydrogen renders the crystals bluish and electrically conductive. Structurally, $MgGa_2O_4$ is more isotropic than Ga_2O_3 since it crystallizes in a cubic unit cell [21], which does not possess the mechanical anisotropy of monoclinic systems. $MgGa_2O_4$ has however the drawback that the low mobility still hinders the application in "true" devices based on TCOs, like gas sensors, Schottky contacts, photodiodes, photodetectors, transistors, etc.

Because $MgGa_2O_4$ can be potentially used in devices, it is necessary to understand its fundamental band structure and how it affects other physical quantities, like electrical conductivity and the optical absorption. For this reason, we carried out angle-resolved photoemission (ARPES) experiments on the valence band and gallium 3*d* core level electrons to determine the band dispersion, the size of the band gap, the presence of the surface states, and of a surface band bending. We find that the as-grown samples are strongly *n* doped, but still in the nondegenerate regime, since the conduction band minimum (CBM) could not be measured. The dispersion in the valence band is small, of about 0.6 eV, and generally in good agreement with our *ab initio* density-functional theory calculations. The latter underestimate the size of the gap by about 50%, a problem that we ascribe to the choice of the local density exchange-correlation functional, as it has been shown to occur in other spinel systems. The binding energy of the Ga 3*d* core levels shifts to lower values when the photoelectron emission angle increases, indicating an upward band bending and therefore a surface depletion layer. A thorough analysis of the core level binding energy by an exact model of the surface band bending revealed its depth dependence and lead to the determination of the effective Debye length and the bulk charge carrier density. Thus we establish a way to determine the *bulk* carrier density by means of ARPES, i.e., a probe of the *surface* electronic states.

II. EXPERIMENTAL AND ANALYSIS DETAILS

The measurements were carried out at the 5m-NIM beamline at Bessy II [22]. Bulk single crystals were grown at the Leibniz Institut für Kristallzüchtung (IKZ) by the Czochralski method as described in detail by Galazka *et al.* in [20] and aligned before the experiments by the Laue method, as described in the Appendixes. The surface was prepared by several sputtering and annealing cycles with argon ions. Since this is the very first ARPES experiment on $MgGa_2O_4$, we show later the effect of the surface preparation parameter on the photoemission spectra. Because $MgGa_2O_4$ becomes insulating if annealed at 600 °C, as observed by Galazka *et al.* [20], we chose to anneal at 500 °C. The spectra were measured down to 18 K and, even at that low temperature, no charge up was observed in the spectra (at a maximal flux of about 10^{11} photons per second), as observed in the data presented in the Appendixes.

To obtain reliable ARPES spectra along the high-symmetry directions of the crystal, the sample has to be aligned to the rotational axes of the manipulator. To accomplish this task, we used the information derived from the Laue diffraction experiments, as thoroughly explained in the Appendixes. This procedure alone is not sufficient to accurately determine the normal emission direction. To determine it, we have used the theoretical calculations shown in Fig. 3. One recognizes that the theoretical valence band maximum is located at the Γ point. We acquired spectra rotating the manipulator about the two perpendicular in-plane axes and thus determining the angles for which the bands have the lowest binding energy, i.e., are at he valence band maximum. These angles determine thus the normal emission direction with sufficient accuracy to carry out the photon-energy dependent ARPES experiments to measure the dispersion along $k_\perp$.

Because of the high angular resolution, 0.2°, of our SES 2002 detector, the line shape of the valence band at a particular point of the Brillouin zone was obtained by integrating the intensity over a small angular range, typically 0.5° or 1°. The complete band dispersions shown in the main paper were obtained joining together spectra measured for which the emission angle was changed stepwise by 10°, since the detector has an acceptance angle of 14°. Of the total acceptance angle, only the central 10° was considered and the 2° on either side were used to check the sample alignment and rotation accuracy, but otherwise not used in the figures presented here. To obtain the band positions, the line shape was fit with a polynomial function in a small range about the maximum. To estimate the band gap, the inflexion point on the low binding energy side of the valence band was found. Then a linear fit of the spectrum was done and the linear function extrapolation to zero yielded the valence band maximum energy. This value was then used to calculate the band gap size.

The dispersion along $k_\perp$ was obtained by using the standard ARPES formula for the calculation of $k_\perp$ as a function of the kinetic energy, which contains the unknown inner potential V_0:

$$k_\perp = \frac{\sqrt{2m}}{\hbar}\sqrt{E_K\cos^2\theta - V_0}, \tag{1}$$

where m is the electron mass, $\hbar$ is the reduced Planck constant, and E_K and θ are the photoelectron kinetic energy and emission angle. For the normal emission direction, $\theta = 0°$.

The inner potential V_0 can be determined, for any crystalline material, using the periodicity of the band structure. In fact, the electronic bands must have maxima or minima at certain high symmetry points of the reciprocal lattice; also those located along the $k_\perp$ direction. Since our $MgGa_2O_4$ sample is oriented with the (001) direction perpendicular to the surface, the reciprocal space points Γ and X can be reached at normal emission using two photon energies and at those two points the band dispersion must show maxima and/or minima. This is readily observed in the data of Fig. 2, where one maximum and one minimum are present.

Using the lattice parameter of $MgGa_2O_4$ in the fcc lattice representation, we have that the X point lies at a distance of $2\pi/a$ from Γ. Furthermore, in the extended zone scheme, the Γ point is at a position $k_\perp^\Gamma = \frac{2\pi}{a}n$, with n even number and, as a consequence, the X lies at $k_\perp^X = \frac{2\pi}{a}(n+1)$. Using the formula (1), one obtains

$$\frac{k_\perp^\Gamma}{k_\perp^X} = \frac{\frac{\sqrt{2m}}{\hbar}\sqrt{E_K^\Gamma\cos^2\theta - V_0}}{\frac{\sqrt{2m}}{\hbar}\sqrt{E_K^X\cos^2\theta - V_0}} = \frac{\sqrt{E_K^\Gamma - V_0}}{\sqrt{E_K^X - V_0}}, \tag{2}$$

where E_K^Γ and E_K^X are the kinetic energies necessary to reach the Γ and X points, respectively, and in the last equality the normal emission condition has been used. Equation (2) can be easily solved to yield the inner potential parameter V_0 as a function of the experimental kinetic energies and of the positions of the high symmetry points Γ and X, which have been derived above. Thus one has

$$V_0 = \frac{\left(\frac{k_\perp^\Gamma}{k_\perp^X}\right)^2 E_K^X - E_K^\Gamma}{\left(\frac{k_\perp^\Gamma}{k_\perp^X}\right)^2 - 1}. \tag{3}$$

In Eq. (3) one notices that the ratio of the $k_\perp$ momenta appears, which equals $\frac{k_\perp^\Gamma}{k_\perp^X} = \frac{\frac{2\pi}{a}n}{\frac{2\pi}{a}(n+1)} = \frac{n}{n+1}$. The last formula shows that the ratio of the $k_\perp$ components of the Γ and X points of the fcc lattice does not depend on the lattice parameter, but only on the integer n, the Brillouin zone order in the extended zone scheme. Thanks to this observation the formula for V_0 simplifies to

$$V_0 = \frac{\left(\frac{n}{n+1}\right)^2 E_K^X - E_K^\Gamma}{\left(\frac{n}{n+1}\right)^2 - 1} = \frac{(n+1)^2 E_K^\Gamma - n^2 E_K^X}{2n+1}. \tag{4}$$

This formula can be used to determine the value of the inner potential as a function of n, which is 11.2 eV for $MgGa_2O_4$.

III. DETAILS OF THE BAND STRUCTURE CALCULATIONS

The calculations presented in this work have been done using the QUANTUM ESPRESSO code [23] implementing the density functional theory using a plane wave ansatz and pseudopotentials. For the calculations, we used an fcc unit cell and the 14 atoms basis. The pseudopotentials used were of the norm-conserving scalar relativistic type, generated by the Fritz-Haber Institute method. For the integration on the

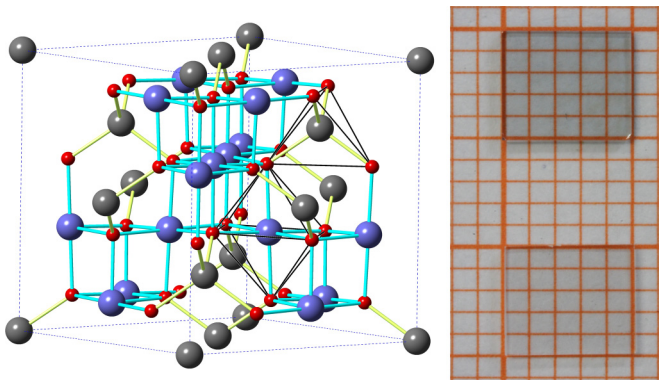

FIG. 1. (Left) Inverse spinel structure of $MgGa_2O_4$ with balls representing the different ions: (red) oxygen anions, (gray) tetragonal cations, and (violet) octahedral cations. Both these coordination sites are marked by the black lines. (Right) $MgGa_2O_4$ wafers prepared from a bulk crystal: insulating (top) and semiconducting (bottom).

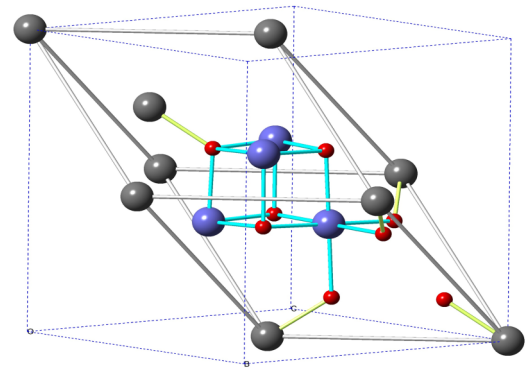

FIG. 2. Structure of $MgGa_2O_4$ in the fcc system with 14 atoms basis. Spheres colored in gray indicate the Ga atoms, in red the oxygen atoms, and in blue either Mg or Ga ions in the tetrahedral sites (see text).

Brillouin zone in the self-consistent calculation a $6 \times 6 \times 6$ Monkhorst-Pack mesh was used and a cutoff of 80 Ry for the wave function, while a 360 Ry cutoff for the charge density is automatically selected by the code. The Perdew-Burke-Erzenhof exchange and correlation functional was used and the experimental values of the atomic positions and the lattice parameter were chosen. The energy cutoff, the lattice parameter, and the atomic positions were changed in order to be sure that the calculations were fully converged and therefore exclude artificial discrepancies between theory and experiment. Virtually no change in the band gap and band energy could be determined upon an increase of the energy cutoff to 400 Ry. A variation of 1% of the lattice parameter yielded the total energy minimum, but showed no improvement in the band gap. The band gap remained also unchanged upon relaxation of the atomic positions. Four configurations of the tetrahedral Ga and Mg site occupations (see next section) were calculated and all showed very similar results, with variation in the band energies of the order of a few meV. Because all the elements in $MgGa_2O_4$ are light, no strong spin-orbit effect is expected and therefore no fully relativistic calculation was attempted.

IV. CRYSTAL STRUCTURE

$MgGa_2O_4$ crystallizes in an inverse spinel structure, which can be described by a simple cubic lattice with parameter $a = 8.286$ Å, as represented in Fig. 1. This representation consists in a unit cell with a basis of 56 atoms, 32 oxygen atoms and 24 cations occupying 16 octahedral sites and eight tetrahedral sites, and was the first one used to classify $MgGa_2O_4$ [21].

This complex structure can be considerably simplified since it possesses the space group of the diamond structure and can be reduced to a cubic face-centered lattice with a 14 atoms basis, namely eight oxygen atoms and six cations (Mg and Ga), as shown in Fig. 2. The main idea is to consider first only the Ga cations: as one can see from Fig. 2(a), these ions sit exactly at the positions of an fcc lattice with one atom basis. The second step is to consider one of the Ga ions sitting at the (3/4, 3/4, 3/4) position, along the (111) direction, inside the primitive fcc unit cell volume. This Ga is surrounded by four oxygens forming a tetrahedron and also included in the fcc primitive unit cell. By a permutation of two fcc unit vectors it is possible to shift oxygens to an equivalent position forming an empty tetrahedron around the (1/4, 1/4, 1/4) position, as shown in Fig. 2. Here, each oxygen is coordinated to a Ga ion and three of those contribute to form the octahedron at which center an Mg or another Ga sit, as indicated in Fig. 2 by the violet spheres. Three further Mg or Ga ions form a tetrahedron, to which four more oxygen are bound, three of which "close" the octahedron and one of which "closes" the tetrahedron.

Thus the large simple cubic unit cell with a basis of 56 atoms can be reduced to a simpler fcc unit cell with 14 atoms: 8 O, 4 Ga, and 2 Mg. The degree of disorder in the inverse spinel unit cell can be further characterized since two Ga atoms must sit in the (0,0,0) and (3/4, 3/4, 3/4) positions. Therefore, in the remaining four tetrahedral sites two Mg and two Ga atoms can be placed. Since there are four possible sites, each of which must be occupied by two (and only two) cations of each species (to maintain charge neutrality), there is a total of $\frac{4!}{2!\times 2!} = \frac{24}{2\times 2} = 6$ possible configurations, each of which breaks locally the inversion symmetry.

In the ideal inverse spinel structure, the gallium ions occupy all tetrahedral sites, while the remaining gallium and by the magnesium ions randomly occupy the octahedral sites. The position of the cations is not fixed, but Mg and Ga can (by temperature activation) hop between octahedral and tetrahedral sites. To characterize this behavior an inversion index can be defined by the percentage of the Ga atoms in the tetrahedral sites. According to first-principles calculations, the possibility for the cations to exchange site originates a phase transition [24] at a temperature of 1300 K and demonstrated experimentally above 800 °C [20,25]. At these high temperatures, the degree of inversion falls up to 2000 K to around 85%. According to Seko *et al.* [24], another phase transition occurs because the Mg and Ga cations at the octahedral sites can exchange their position. This process induces a transition at a temperature of 270 K, as calculated in [24], at which the structure changes from cubic to tetragonal.

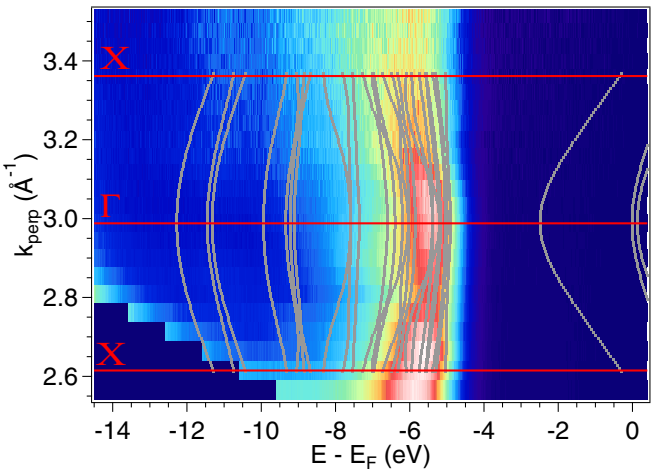

FIG. 3. $k_\perp$ dispersion represented by energy distribution curves stacked as a color map and overlapped to the *ab initio* band structure calculations, represented by the gray dotted lines. The horizontal red lines indicate the Γ and X high-symmetry points of the Brillouin zone.

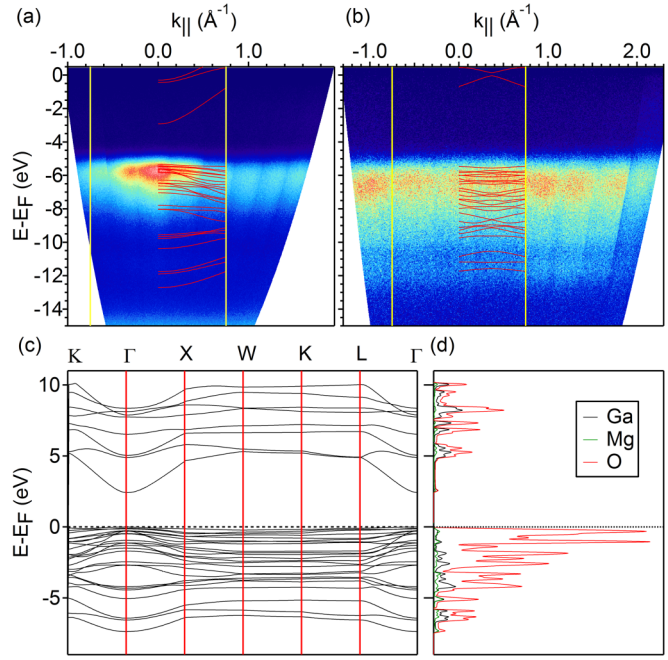

FIG. 4. (a) ARPES maps at $h\nu = 26$ eV (Γ-X direction) and (b) $h\nu = 39$ eV (X-W direction) overlapped to the theoretical band structure, shifted by 5.34 eV. The theoretical CBM energy is too low: the theoretically predicted gap is too small. (c) The full theoretical band structure plotted along the high symmetry directions of the fcc Brillouin zone, labeled by the high-symmetry points. (d) Orbital decomposition of the density of states of $MgGa_2O_4$.

V. EXPERIMENTAL BAND DISPERSION AND COMPARISON TO THEORY

By measuring the ARPES spectra at different photon energies and normal emission, as shown in Fig. 3, we obtained the band dispersion along the momentum direction perpendicular to the surface, namely the ΓX direction. The intensity map indicates that the highest peak is located about 5.2 eV below the Fermi level and its position changes as a function of the perpendicular component of wavevector, a clear signature of the bulk character of the band. Using the procedure explained in Sec. II, we determine that with $h\nu = 26$ eV the Γ point is reached and with 39 eV the X point, which are the fcc Brillouin zone edges. Close inspection of the data in Fig. 3 reveals that the total bandwidth is about 600 meV, small with respect to the 6 eV total width of the full valence band, but not negligible. Moreover, the experimental dispersion is in full agreement with the band structure calculations, which overlap the experimental bands, as shown in Fig. 3.

Since $MgGa_2O_4$ is a nondegenerate semiconductor, it is not possible to provide the value of the band gap because the CBM is unoccupied and therefore not observable by ARPES. Data along one in-plane Γ-X direction are shown in Fig. 4, where a clear dispersion about Γ can be observed. The theoretical calculations, superimposed to the data, reproduce the experiment well and show generally flat bands, with a downward (negative effective mass) dispersion. While the individual theoretical bands cannot be experimentally resolved, it is possible to observe a separate manifold of bands at about −12 eV along both ΓX and XM directions having an experimental effective mass higher than the theoretical one.

Although the overall theoretical band dispersion is in agreement with the experimental one, the calculated band gap is 2.45 eV, i.e., about half of the experimental one, 4.9 eV [20]. This strong disagreement is readily observed in the top-left panel of Fig. 4, in which the CBM lies too low in energy, within the experimental ARPES band gap. However, no state in the band gap was measured by photoemission and we attribute this finding to the common underestimation of the band gap occurring in density-functional theory (DFT) calculations, when done in the local-density approximation, as in the present case. Calculations of a higher level of sophistication could solve the problem in $MgGa_2O_4$ and reproduce the correct size of the band gap. The dependence of the theoretical band gap on the choice of the exchange-correlation functionals in spinels was actually addressed in theoretical papers [26,27] for several spinels like $MgGa_2O_4$. The calculations in these works yield a band gap that is at most 66% the size of the experimental one when done within the local approximation, while the modified Becke-Johnson functional or the GW approach widens the band gap to 95% of the experimental one.

From the spectra of Fig. 4 the general trend of the band dispersion is obvious and a bandwidth of about 500 meV, very similar to that of the dispersion along $k_\perp$ (in Fig. 3), can be recognized. A measurement along the X-M direction was performed and presented in Fig. 4(b) and there it is possible to see a weaker dispersion. In all cases, no intensity could be observed at the Fermi level. Since the latter is usually observed if surface defects are present, we conclude that the density of surface defects in sputtered and annealed $MgGa_2O_4$ is below the detection limit of ARPES.

The theoretical calculations predict that $MgGa_2O_4$ is a direct semiconductor, since the CBM lies at the Γ point. If we assume that the theoretical *position* of the CBM is correct, as in the case of Ga_2O_3, In_2O_3 [15], and $MgAl_2O_4$ [26], then we deduce that for ARPES $MgGa_2O_4$ has a direct band gap. This is shown in Fig. 4, where one can observe that the experimental

top of valence band and the theoretical CBM lie at the Γ point. Figure 4(d) shows the contribution of each constituent to density of states of $MgGa_2O_4$. One observes that the valence band is dominated by oxygen states, especially near the valence band maximum, with the metal cation contribution becoming sizable only at higher binding energies. This is also the situation in the conduction band, where the metal and oxygen weights are comparable at all energies.

VI. EXACT MODEL OF THE BAND BENDING

Lüth [28,29] presents an exact one-dimensional model of the band bending in which no assumption is made on the depth and width of the accumulation/depletion region and if it is deep enough to originate a free electron gas. It only considers the bulk doping and how much the bands have to bend at the surface in order to keep the Fermi level constant across the semi-infinite solid. We report here the main derivation steps and the numerical results important for the present work.

The depth-dependent potential, $v(z)$, normalized to the thermal excitation energy,

$$v(z) = \frac{eV(z)}{k_B T}, \tag{5}$$

is subject to the Laplace equation:

$$\frac{d^2v}{dz^2} = -\frac{e^2}{k_B T \epsilon \epsilon_0}(n_b - p_b + p_b e^{-v} - n_b e^{v}). \tag{6}$$

The intrinsic potential u_b is the potential in the bulk, asymptotically away from the surface, while n_b and p_b are the density of bulk donors and acceptors.

The first integration of the above equation can be done analytically yielding the following expression:

$$\frac{z}{L} = \int_{v_s}^{v} \pm \frac{dv}{\sqrt{2}\sqrt{\frac{\cosh u_b + v}{\cosh u_b} - v \tanh u_b - 1}}, \tag{7}$$

an implicit equation for the normalized potential. To obtain it, one has to resort to numerical integration leading to the band-bending potential, which can either be of accumulation, depletion, or inversion type. The results of the integration for various values of u_b are shown in Fig. 5.

The first important point in the last equation is that the depth is scaled to the effective Debye length L of the solid:

$$L = \sqrt{\frac{\epsilon \epsilon_0 kT}{e^2(n_b + p_b)}}, \tag{8}$$

where e is the elementary electron charge, ϵ_0 is the vacuum permittivity, and k_B is the Boltzmann constant. L is a function of temperature, dielectric constant, and of the charge doping under the square root. The second important point is that when the normalized surface potential becomes high, the band bending acquires a linear dependence on the normalized depth over at least a depth of $2L$. In this limiting case,

$$v(z) = v_s - 7 \times \frac{z}{L}, \tag{9}$$

where the proportionality constant has been derived from Fig. 5. This linear decay is important for $MgGa_2O_4$, as it will be explained in the next section.

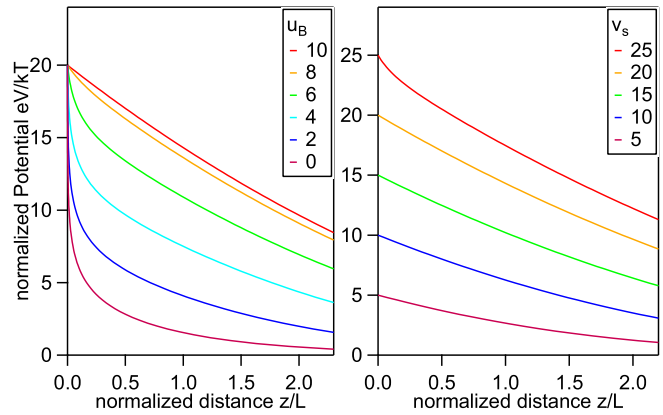

FIG. 5. Calculation of the band bending potential at semiconductor surfaces for different surface potentials v_s and intrinsic potentials u_b, as indicated in the labels of the two panels.

VII. Ga 3*d* CORE LEVELS

The Ga 3*d* core levels can be observed at a binding energy of $E_B = 21.6$ eV. In our measurements, only one peak was observed, even though spin-orbit coupling should split it in at least two components. The most important feature of the core level data is that the binding energy is reduced by about 350 meV upon increase of the photoelectron emission angle, as shown Fig. 6, while no change is expected at all. The observation of a change in binding energy can be attributed to the depth-dependent band bending occurring near the surface. At fixed kinetic energy, i.e., fixed photoelectron escape depth, the angular dependence of the binding energy corresponds indeed to a depth sensitivity, whose quantitative relation is illustrated in the Appendixes.

We used the exact model exposed in the previous section to retrieve the depth dependence of the band bending from

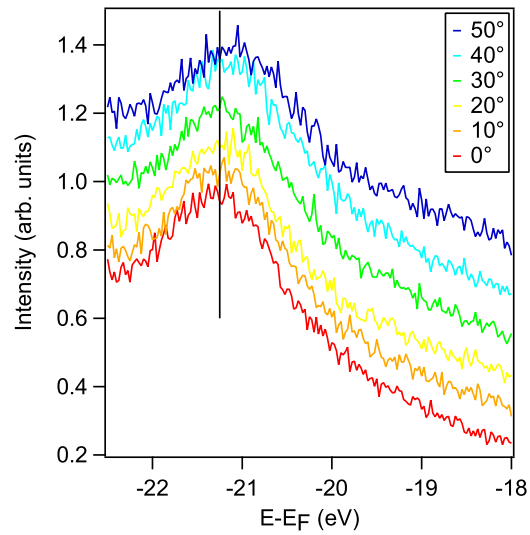

FIG. 6. Angle-resolved photoemission spectra of the Ga 3*d* core levels taken at the angles indicated in the label. A black vertical line indicates the peak maximum at normal emission (labeled 0°). A clear shift of the peak is observed when the photoelectrons are observed at grazing emission.

the experimental core-level data. We used the experimental dielectric constant of bulk $MgGa_2O_4$, which has been measured as a function of the temperature [30] and attains a value of $\epsilon = 9.4$ at room temperature. The effective Debye length can be calculated using the angular dependence of the Ga $3d$ peak position, as explained in the Appendixes. Therefore, the bulk carrier density can be estimated in 3×10^{17} cm^{-3}, which is in good agreement with Hall-effect measurements [20], which are bulk sensitive. A significant advantage of the ARPES with respect to the transport experiments is that in the former ordinary contacts of Mo and Ta were used to ground the sample, while in the latter the sample contacts had to necessarily be made of a special InGa alloy and capacitance discharge. The photoemission spectra showed no sign of electrical charge-up effect (as shown in the Appendixes) on photon flux variation of a factor of about 20 both at room temperature and at 18 K also indicating that $MgGa_2O_4$ undergoes no Anderson localization and retains its semiconducting character throughout the temperature range explored.

Therefore, with the method presently proposed, a reliable value of the bulk carrier density can be estimated by ARPES, with no need of special grounding contacts. While not in general justified, the use of a bulk model to interpret ARPES data is in the present case possible because the experiments showed no evidence of surface states (all bands show a $k_\perp$ dispersion) and no surface defect states in the band gap. Under these conditions, using the bulk model leads to reliable estimates of the material-specific parameters.

Theoretical model calculations of the Debye length [31] for highly doped GaAs, but still in the nondegenerate regime, predict a very peculiar dependence on temperature and doping. For a very thorough presentation of the theory of the Debye length in bulk and nanostructured semiconductors, see Ref. [32]. While with increasing carrier concentration the Debye length generally decreases, if the Fermi level crosses the conduction band, then the Debye length can acquire values as large as 100 Å in a narrow temperature range. Although the model calculations [31] were done for doped GaAs, the value of the Debye length obtained at room temperature and for a doping of 5×10^{17} cm^{-3} is about 60 Å, which is remarkably close to the value obtained from our photoemission experiments on $MgGa_2O_4$. Despite the difference between GaAs and $MgGa_2O_4$, our results are very promising and the temperature dependence of the Debye length in transparent oxides by ARPES are planned for the near future.

VIII. TEMPERATURE DEPENDENCE

Figure 7 shows photoemission spectra taken at two points of the Brillouin zone with two photon energies at different temperatures. The first important feature the data show is that the band gap remains virtually constant, with a variation of a few meV over the whole temperature range. Since there is no state in the band gap, we have no access to the sample Fermi level. However, an energy scale reference can be made by means of the core-level data, as shown in the right panel of Fig. 7, where close inspection reveals a slight shift down to 100 K.

The most prominent variation caused by the temperature is in the valence band line shape at the Γ point, where the intensity

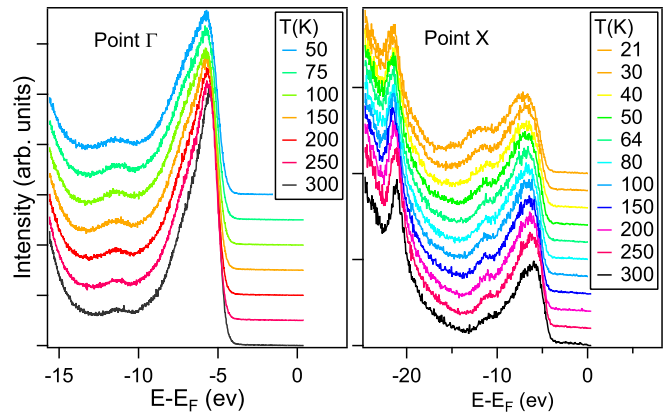

FIG. 7. Temperature-dependent change of the (left) valence band at $h\nu = 26$ eV corresponding to the Γ point, averaged over 2° about the normal emission direction; (right) $3d$ core levels and the valence band, averaged over 4° at a photon energy $h\nu = 39$ eV corresponding to the X point.

ratio of the main peak at −5.5 eV and of its shoulder at −7 eV change continuously from 300 K to 50 K. This continuous variation cannot confirm the theoretical prediction of a phase transition of Seko *et al.* [24], which predicts that the order parameter has a jump at about 270 K and remains constant at lower temperatures. A phenomenon that could explain the continuous change of the valence band line shape is the temperature dependence of the lattice parameter, which is unfortunately experimentally unknown in the low-temperature range.

IX. CONCLUSION

In this article, we have presented a comprehensive theoretical and experimental investigation of the electronic structure of n-doped intrinsic $MgGa_2O_4$. ARPES spectra were measured with low-energy photons in the UV regime and by means of photon energy- and angle-resolved scans. We were able to map the electronic structure of the material along two different high-symmetry directions. Furthermore, ARPES showed neither surface states nor defect-related nondispersive features in the band gap. The measured band dispersion is consistent with our *ab initio* DFT calculations, with the exception of the conduction band minimum, whose energy is too low, an effect of the underestimation of the gap size by DFT done in the local-density approximation.

An experimental core-level binding energy shift versus the photoelectron emission angle is a clear indication of a band bending in the material. We analyzed it in terms of an exact model, which leads to the determination of the material effective Debye length and the bulk carrier concentration. Remarkably, these two quantities have been obtained by a surface-sensitive method, ARPES. Even more surprising is the fact that $MgGa_2O_4$ retained its semiconducting character down to a temperature of 20 K, with no sign of charge up in the photoemission spectra.

We obtained a good agreement between values of the carrier density determined by ARPES and by transport measurements and also between the experimental ARPES value of the Debye length and model calculations, the latter showing a strong

temperature dependence. Our results indicate a way to quantify these two quantities in nondegenerate semiconductors by means of spectroscopic surface-sensitive methods.

ACKNOWLEDGMENTS

M.M. thanks O. Pawlinski of Helmholtz-Zentrum-Berlin (HZB) for the technical support. We also thank Dr. K. Irmscher for the discussion and critical review of our manuscript. This work was performed in the framework of GraFOx, a Leibniz-Science Campus partially funded by the Leibniz Association.

APPENDIX A: SAMPLE PREPARATION AND CHARGING EFFECTS

The samples were prepared by sputtering and annealing, although cleavage was tried, but turned out to be impossible. We used argon ions accelerated to 1 keV at a partial pressure of 4×10^{-5} mbar for one hour. The annealing was carried out at 500 °C to reorder the crystal surface, also for one hour. The quality of the spectra increased quickly with sputtering and annealing cycles, as it can be seen from Fig. 8. As also shown in the top part of Fig. 8, the surface is quite robust to contaminations, since the main peak intensity decreases about 20% in 3 days from the preparation, with no new feature detectable.

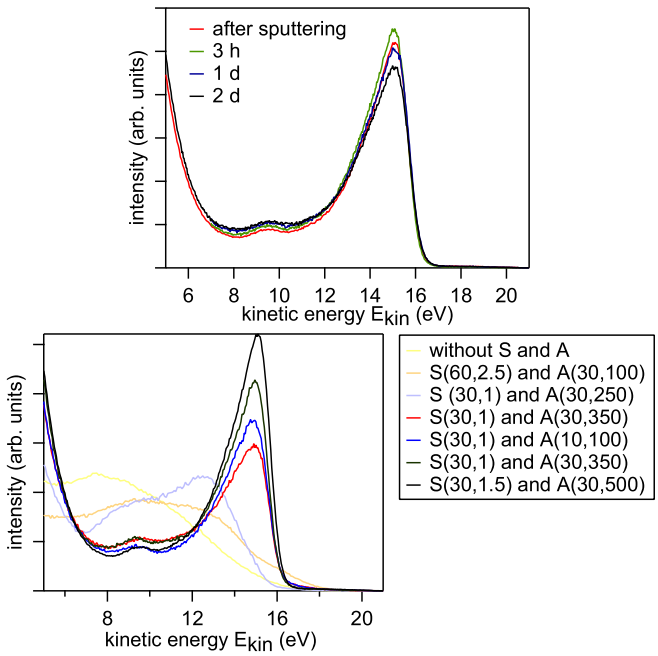

FIG. 8. (Top) Examples of the valence band at the Γ point measured at different times: (red line) fresh surface right after the preparation, (green line) 3 h after the preparation, (blue line) 1 day after the preparation, and (black line) 3 days after the preparation. (Bottom) Examples of spectra taken at the beginning of the experiment to show the improvement of the surface quality upon sputtering and annealing. In the figure label, the sputtering parameters are indicated by $S(t, E)$, with t indicating the sputtering time in minutes and E indicating the ion energy in keV. Similarly, the annealing parameters are indicated by $A(t, T')$, with t giving the annealing time and T' the annealing temperature.

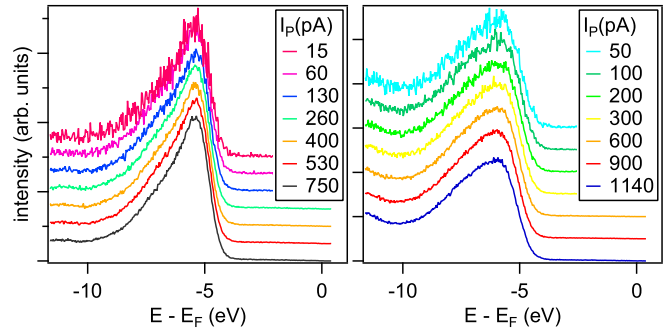

FIG. 9. Temperature dependence of the photoemission spectra taken at normal emission under different illumination intensities (referenced to the mirror current) (left) at 300 K and (right) at 18 K. No shift in the spectra is visible, indicating no charge-up effects.

We found no charging of the samples during the measurements as indicated by the photon intensity-dependent valence band spectra at 18 K (right) and at 300 K (left) of Fig. 9. The photon intensity was referenced to the drain current from the last mirror of the beamline before the sample. No apparent shift of the spectra was observed, which would occur with a charging sample.

APPENDIX B: LAUE MEASUREMENTS

To exactly map the electronic structure by ARPES, it is necessary to find the high symmetry directions with respect to the crystal edges. Therefore, a Laue diffraction measurement was performed and the result is shown in Fig. 10. The image shows a clear fourfold symmetry resulting from the (001) axis being perpendicular to the surface (and parallel to the x-ray beam). The diffraction intensity was calculated using the standard diffraction amplitude formula:

$$S = \sum_i f_i e^{2\pi i(hu_i + kv_i + lw_i)}, \tag{B1}$$

where hkl stands for the Laue indices, which are Miller indices or an integer multiple, uvw indicates the position of the ith

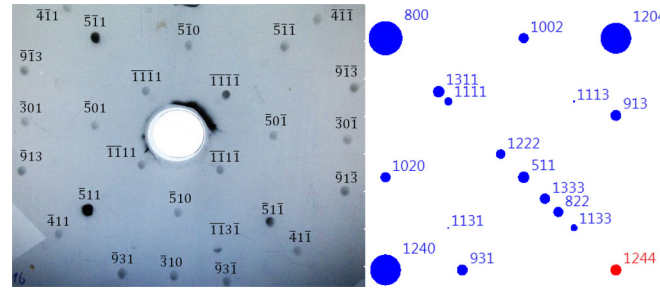

FIG. 10. (Left) Experimental Laue diffraction image of $MgGa_2O_4$ done with an x-ray tube equipped with a Cu target. (Right) Theoretical calculation of the Laue diffraction pattern (see main text for details). Each diffraction spot is labeled with the Miller indices of the corresponding crystal planes and the radius of the circle is proportional to the theoretical intensity. The (800) diffraction spot is at the origin of the axes and the $(\bar{5}01)$ point in the experimental figure (left) corresponds to the (1020) in the theoretical calculation (right). Similarly the $(\bar{3}10)$ corresponds to the (1240) point.

atom in the unit cell, and f_i is the atomic structure factor of the atom i. The structure factors were taken from [33].

Since all atomic positions are known, the diffraction intensity can be calculated at any point of the reciprocal space and, as shown in Fig. 10, the calculations, done for the fcc lattice representation, reproduce all experimental diffraction points and the agreement is excellent. This procedure yielded the correct alignment needed for the ARPES measurements.

APPENDIX C: CORE LEVELS, ESCAPE DEPTH, AND BAND BENDING

It is very well known that, in absence of a band bending, like in metals or very pure semiconductors and/or in absence of specific surface defects, the binding energy of core levels should not depend on the depth. Another well-known fact is that the photoelectron inelastic mean free path λ_e, the origin of ARPES surface sensitivity, is finite and short, i.e., comparable to the thickness of a few monolayers. Thus an experimental dependence of the core-level binding energy on the emission angle is a direct evidence of a potential shifting the energy positions, i.e., a band bending occurring at the surface.

In the present case, the Ga $3d$ core level binding energy of 21.6 eV reduces with increasing (becoming more grazing) emission angle. This effect is attributed to an upward band bending occurring near the surface and in a depth range comparable to λ_e. The attenuation of the excited photoelectrons traveling to the surface can be calculated with the usual (Lambert) formula:

$$I_a(E_{\rm ph}, E_{\rm kin}, z) = I_e e^{-\frac{z}{\lambda_e(E_{\rm kin})\cos\phi_e}}. \tag{C1}$$

The total number of photoelectrons reaching vacuum can be simplified by

$$I_a \approx e^{-za} \Rightarrow a = \frac{1}{\lambda_{\rm eff}} = \frac{1}{\lambda_e(E_{\rm kin})\cos\phi_e}, \tag{C2}$$

where an effective inelastic mean free path has been introduced.

The core-level energies shift because of the band bending under the surface in a depth-dependent way, which we explained in the previous section. In full generality, the measured binding energy $E_M(a)$ at an angle α is a weighted mean of the depth-dependent core-level binding energies $E_C(z)$. The weights are given by the exponential in Eq. (9) which depends on the depth under the surface and the effective inelastic mean free path λ_e:

$$E_M(a) \approx \frac{\sum_{z=0}^{\infty} E_C(z) e^{-z\cdot a}}{\int_{z=0}^{\infty} e^{-z\cdot a}} \approx \frac{\int_0^{\infty} E_C(z) e^{-z\cdot a} dz}{\int_0^{\infty} e^{-z\cdot a} dz}. \tag{C3}$$

The first expression for $E_M(a)$ involves a sum instead of an integral because the positions of the emitting atoms are discrete inside any actual material. They can be indexed by a natural number and the interlayer distance. This term has been approximated by a continuous limit in order to use the model of the previous section.

The shift of the core levels caused by the band bending is assumed to be of the form of $E_C(z) = E_0 + A\, e^{-Bz}$, a simple exponential, which has as a particular case the linear dependence. With this approximation, Eq. (7) can be solved and we obtain the following formula for the band bending as a function of $a = 1/\lambda_{\rm eff}$:

$$E_M(a) = \frac{\frac{E_0}{a} + \frac{A}{a+B}}{\frac{1}{a}} = E_0 + \frac{A}{1+\frac{B}{a}} = E_0 + \frac{A}{1 + B\cdot\lambda_{\rm eff}}. \tag{C4}$$

Using the linear approximation of the band bending, $E_C(z) = A + Bz$, leads to

$$E_M(a) = A + \frac{B}{a} \approx A + B\cdot\lambda_e\cos\phi_e. \tag{C5}$$

In our measurement, we observe an increase in the binding energy of $B\lambda_e \approx 0.5$ eV in the angular range that we used. This value is the last parameter we need to calculate the effective Debye length, assuming $\lambda_e \approx 5$ Å,

$$L = \frac{7}{0.5}\lambda_e \approx 70\ \text{Å}. \tag{C6}$$

Once the value of the effective Debye length is known, the bulk carrier density can be estimated, as shown in the previous section:

$$n_b + p_b = \frac{\epsilon\epsilon_0 k_B T}{e^2 L^2} \approx 2\times 10^{17}\frac{1}{\text{cm}^3}. \tag{C7}$$

The value we obtain is reasonable, i.e., it is a typical value for unintentionally doped transparent conducting oxide crystals, which also have the same color as our $MgGa_2O_4$.

[1] R. A. Powell, W. E. Spicer, and J. C. McMenamin, Phys. Rev. B **6**, 3056 (1972).

[2] K. Ozawa, Y. Oba, K. Edamoto, M. Higashiguchi, Y. Miura, K. Tanaka, K. Shimada, H. Namatame, and M. Taniguchi, Phys. Rev. B **79**, 075314 (2009).

[3] L. F. J. Piper, A. R. H. Preston, A. Fedorov, S. W. Cho, A. DeMasi, and K. E. Smith, Phys. Rev. B **81**, 233305 (2010).

[4] R. Yukawa, K. Ozawa, S. Yamamoto, H. Iwasawa, K. Shimada, E. F. Schwier, K. Yoshimatsu, H. Kumigashira, H. Namatame, M. Taniguchi, and I. Matsuda, Phys. Rev. B **94**, 165313 (2016).

[5] P. D. C. King, T. D. Veal, C. F. McConville, J. Zuniga-Pérez, V. Munoz-Sanjosé, M. Hopkinson, E. D. L. Rienks, M. F. Jensen, and Ph. Hofmann, Phys. Rev. Lett. **104**, 256803 (2010).

[6] J. J. Mudd, T.-L. Lee, V. Munoz-Sanjosé, J. Zuniga-Pérez, D. Hesp, J. M. Kahk, D. J. Payne, R. G. Egdell, and C. F. McConville, Phys. Rev. B **89**, 035203 (2014).

[7] J. J. Mudd, T.-L. Lee, V. Munoz-Sanjosé, J. Zuniga-Pérez, D. J. Payne, R. G. Egdell, and C. F. McConville, Phys. Rev. B **89**, 165305 (2014).

[8] K. H. L. Zhang, R. G. Egdell, F. Offi, S. Iacobucci, L. Petaccia, S. Gorovikov, and P. D. C. King, Phys. Rev. Lett. **110**, 056803 (2013).

[9] C. Körber, V. Krishnakumar, A. Klein, G. Panaccione, P. Torelli, A. Walsh, J. L. F. Da Silva, S.-H. Wei, R. G. Egdell, and D. J. Payne, Phys. Rev. B **81**, 165207 (2010).

[10] V. Scherer, C. Janowitz, A. Krapf, H. Dwelk, D. Braun, and R. Manzke, Appl. Phys. Lett. **100**, 212108 (2012).
[11] W. Meevasana, P. D. C. King, R. H. He, S-K. Mo, M. Hashimoto, A. Tamai, P. Songsiriritthigul, F. Baumberger, and Z.-X. Shen, Nat. Mater. **10**, 114 (2011).
[12] A. F. Santander-Syro, O. Copie, T. Kondo, F. Fortuna, S. Pailhès, R. Weht, X. G. Qiu, F. Bertran, A. Nicolaou, A. Taleb-Ibrahimi, P. Le Fèvre, G. Herranz, M. Bibes, N. Reyren, Y. Apertet, P. Lecoeur, A. Barthélémy, and M. J. Rozenberg, Nature (London) **469**, 189 (2011).
[13] M. Mohamed, C. Janowitz, I. Unger, R. Manzke, Z. Galazka, R. Uecker, R. Fornari, J. R. Weber, J. B. Varley, and C. G. Van de Walle, Appl. Phys. Lett. **97**, 211903 (2010).
[14] M. Mohamed, I. Unger, C. Janowitz, R. Manzke, Z. Galazka, R. Uecker, and R. Fornari, J. Phys.: Conf. Ser. **286**, 012027 (2011).
[15] C. Janowitz, V. Scherer, M. Mohamed, A. Krapf, H. Dwelk, R. Manzke, Z. Galazka, R. Uecker, K. Irmscher, R. Fornari, M. Michling, D. Schmeißer, J. R. Weber, J. B. Varley, and C. G. Van de Walle, New J. Phys. **13**, 085014 (2011).
[16] M. Mohamed, K. Irmscher, C. Janowitz, Z. Galazka, R. Manzke, and R. Fornari, Appl. Phys. Lett. **101**, 132106 (2012).
[17] M. Higashiwaki, K. Sasaki, A. Kuramata, T. Masui, and S. Yamakoshi, Appl. Phys. Lett. **100**, 013504 (2012).
[18] Courtesy of Dr. M. Higashiwaki, NICT, and also available at https://www.nict.go.jp/press/2012/01/05-1.html; http://www2.nict.go.jp/green/.
[19] J. Åhman, G. Svensson, and J. Albertsson, Acta Crystallogr., C **52**, 1336 (1996).
[20] Z. Galazka *et al.*, Phys. Status Solidi A **212**, 1455 (2015).
[21] J. E. Weidenborner *et al.*, Acta Crystallogr. **20**, 761 (1966).
[22] C. Janowitz, T. Zandt, L. Dudy, R. Manzke, and G. Reichardt, Nucl. Instrum. Methods, Phys. Res. A **693**, 160 (2012).
[23] P. Giannozzi, S. Baroni, N. Bonini, M. Calandra, R. Car, C. Cavazzoni, D. Ceresoli, G. L. Chiarotti, M. Cococcioni, I. Dabo, A. Dal Corso, S. de Gironcoli, S. Fabris, G. Fratesi, R. Gebauer, U. Gerstmann, C. Gougoussis, A. Kokalj, M. Lazzeri, L. Martin-Samos, N. Marzari, F. Mauri, R. Mazzarello, S. Paolini, A. Pasquarello, L. Paulatto, C. Sbraccia, S. Scandolo, G. Sclauzero, A. P. Seitsonen, A. Smogunov, P. Umari, and R. M. Wentzcovitch, J. Phys.: Condens. Matter **21**, 395502 (2009).
[24] A. Seko, K. Yuge, F. Oba, A. Kuwabara, and I. Tanaka, Phys. Rev. B **73**, 184117 (2006).
[25] L. Schwarz, Z. Galazka, T. M. Gesing, and D. Klimm, Cryst. Res. Technol. **50**, 961 (2015).
[26] P. D. Borges, J. Cott, F. G. Pinto, J. Tronto, and L. Scolfaro, Mater. Res. Express **3**, 076202 (2016).
[27] H. Dixit, N. Tandon, S. Cottenier, R. Saniz, D. Lamoen, B. Partoens, V. van Speybroeck, and M. Waroquier, New J. Phys. **13**, 063002 (2011).
[28] H. Lüth, *Solid Surfaces, Interfaces and Thin Films*, 6th ed. (Springer-Verlag, Berlin, 2015).
[29] A. Many, Y. Goldstein, and N. B. Grover, *Semiconductor Surfaces* (North-Holland, Amsterdam, 1965).
[30] S. Wu, J. Xue, R. Wang, and J. Li, J. Alloy Compd. **585**, 542 (2014).
[31] K. P. Ghatak, A. K. Chowdhury, S. Ghosh, and A. N. Chakravarti, Czech. J. Phys. B **30**, 925 (1980).
[32] K. P. Ghatak and S. Bhattacharya, *Debye Screening Length, Effects of Nanostructures Materials* (Springer-Verlag, Berlin, 2014).
[33] *International Tables for Crystallography* (John Wiley and Sons Ltd, New York, 2006), Vol. C, Chap. 6.1, pp. 554–595.